Proceedings of the CTD/WIT 2019
PROC-CTD19-012
October 15, 2019

Randomized Computer Vision Approaches for Pattern Recognition in Timepix and Timepix3 Detectors

Petr Mánek[1], Benedikt Bergmann[1], Petr Burian[1,2],
Lukáš Meduna[1], Stanislav Pospíšil[1], Michal Suk[1]

On behalf of
[1]*Institute of Experimental and Applied Physics*
Czech Technical University, Prague, Czech Republic
and
[2]*Faculty of Electrical Engineering,*
University of West Bohemia, Pilsen, Czech Republic

ABSTRACT

Timepix and Timepix3 are hybrid pixel detectors (256×256 pixels), capable of tracking ionizing particles as isolated clusters of pixels. To efficiently analyze such clusters at potentially high rates, we introduce multiple randomized pattern recognition algorithms inspired by computer vision. Offering desirable probabilistic bounds on accuracy and complexity, the presented methods are well-suited for use in real-time applications, and some may even be modified to tackle trans-dimensional problems. In Timepix detectors, which do not support data-driven acquisition, they have been shown to correctly separate clusters of overlapping tracks. In Timepix3 detectors, simultaneous acquisition of Time-of-Arrival (ToA) and Time-over-Threshold (ToT) pixel data enables reconstruction of the depth, transitioning from 2D to 3D point clouds. The presented algorithms have been tested on simulated inputs, test beam data from the Heidelberg Ion therapy Center and the Super Proton Synchrotron and were applied to data acquired in the MoEDAL and ATLAS experiments at CERN.

PRESENTED AT

Connecting the Dots and Workshop on Intelligent Trackers (CTD/WIT 2019)
Instituto de Física Corpuscular (IFIC), Valencia, Spain
April 2-5, 2019

1 Introduction

Timepix [15] are hybrid pixel detectors developed by the Medipix collaboration, CERN *. They are comprised of a semiconductive sensor layer, uniformly divided into a square matrix of 256×256 pixels with 55 μm pitch. Timepix3 [19] are successor models of Timepix. Keeping the same pixel layout, they offer superior resolution of time and energy. While Timepix are operated in frame-based mode, producing 2D images integrated over the data acquisition period, Timepix3 also support event-based readout, wherein the detector asynchronously reports hits when they are observed. Detectors of the Timepix family have variety of applications in life sciences [12] and hadron therapy [10]. With great promise for space radiation monitoring [7], Timepix-based systems were mounted at ISS [22, 21] and on board the SATRAM orbital platform [3, 9]. To help characterize mixed radiation fields, Timepix and Timepix3 detector networks were installed at the ATLAS [2] and MoEDAL [18], experiments at the Large Hadron Collider. In all of the listed applications, researchers relied on automated methods to efficiently analyze large quantities of measured data.

Prior to analysis, outputs of the data acquisition process are usually aggregated. While Timepix3 data only require reordering, Timepix frames are subdivided into characteristic patterns called *clusters*, each corresponding to a hit. Since often a multitude of clusters of various shapes are present in a single frame, their segmentation and classification poses a non-trivial task, which is crucial to any subsequent work. In the past, clusters were processed morphologically [11], relying on connectivity-checking algorithms (e.g. Flood Fill) to isolate clusters as spatially localized groups of active pixels, and producing classifications by thresholding on various morphological properties (e.g. linearity, convex hull, etc.). This however imposes additional constraint on the sparsity of processed frames, expecting that only pixels corresponding to common incidence events may be assumed to be spatially adjacent.

The sparsity requirement is often easily satisfied by tuning acquisition duration with respect to observed frame occupancy. This procedure may however pose a challenge in unpredictable and high-flux environments (e.g. in space). In addition, for short frame durations data acquisition is dominated by the constant dead time of 11 ms, during which pixel data are read out and the detector is not sensitive. Having been originally developed for predecessor detectors capable only of binary discrimination in each pixel, morphological segmentation may also be viewed as inherently suboptimal: with quantized intensity information available in Time-over-Threshold (ToT) mode, Timepix frames are reduced to binary images, effectively thresholding intensity values and resulting in precision loss. With that in mind, the main objective of this work is to introduce novel analysis methods suitable for use as alternatives to conventional morphological approaches.

2 Methods

This contribution proposes new analysis methods for Timepix and Timepix3 data, often inspired by recent developments in the field of computer vision. Unlike their morphological counterparts, these approaches may be considered advantageous since they do not require thresholding of intensities at input, and can thus potentially achieve better accuracies [20]. In addition, such algorithms usually posess desirable complexity properties or offer adjustable trade-off between complexity and accuracy (useful e.g. for real-time processing of camera frames). The presented methods are based on robust algorithms which have been shown to reliably diminish adverse effects of input noise, often in relatively large quantities.

In order to apply such methods to Timepix data, frames are effectively treated as images, where pixel intensity refers to the amount of deposited energy (in keV) calibrated from quantized ToT values [13]. Cluster segmentation can then be viewed as an object detection task. With that in mind, this work focuses primarily on a specific class of high energy transfer events constituted by heavy ions.

Timepix clusters produced by heavy ions (shown in Figure 1) are usually labeled as heavy tracks or heavy blobs by morphological classification. Conventionally, three regions of interest are distinguished: (1) a high-energy linear core carrying trajectory information, (2) a surrounding low-energy halo and (3) a multitude of δ-rays probabilistically emitted from the core outwards.

*https://medipix.web.cern.ch/

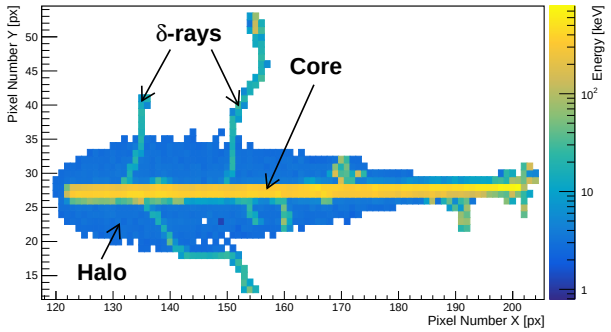

Figure 1: Cluster corresponding to Ar ion at 75 GeV/c with characteristic regions annotated.

2.1 Randomized Trajectory Fitting

The first presented method efficiently estimates the spatial parameter model of the particle trajectory by means of randomized fitting. It is based on the well-known RANSAC algorithm [8]. RANSAC has been shown to possess robust behavior and advantageous complexity properties, in some cases even reaching processing rates suitable for real-time computer vision applications. Since each iteration of the algorithm represents an independent instance of random sampling, the total number of iterations is related to the expected probability of a correct sampling. Given a desired confidence threshold, this conveniently allows to assess fit quality at runtime, enabling early termination once a sufficient fit quality is reached.

Due to the large momentum of heavy ions, a linear trajectory can be assumed (i.e. a line segment). Fit parameters are two planar points $\vec{a}, \vec{b} \in \mathbb{R}^2$ representing the entry point and the exit point of the particle trajectory in the sensor layer, respectively. Within a set of hit pixels, a sampled subset of size 2 is required to fully determine an instance of such model. To formally define the fitting optimization task, energy maximizer formulation is used. The goal is to maximize the utility:

$$U_{w,\Phi}(\mathcal{M} \mid F) = \int_{s=0}^{1} \int_{t=-t_{\max}}^{t_{\max}} w(|t|)\Phi(f_F((1-s)\vec{a} + s\vec{b} + t\vec{n}))dtds. \tag{1}$$

Here, $t_{\max}$ is a sufficiently large distance (e.g. cluster diameter), $\vec{n}$ is a normalized 2D vector orthogonal to $\vec{b} - \vec{a}$, $f_F : \mathbb{R}^2 \to \mathbb{R}_0^+$ is a Timepix frame image function, $w : \mathbb{R}_0^+ \to [0, 1]$ is a distance weight function and $\Phi : \mathbb{R}_0^+ \to \mathbb{R}$ is an energy kernel function.

For the purpose of comparison, three RANSAC-inspired algorithms were developed. Their general scheme is given by Algorithm 1. The proposed algorithms are labeled as follows:

RANSAC Conservative implementation, wherein sampled pixels are directly used for model fitting.

LO-RANSAC Extension of RANSAC which attempts to improve new models using greedy local optimizer.

SA-RANSAC Extension of LO-RANSAC, wherein simulated annealing is used to accelerate computationally intensive local optimization process [14].

2.2 Decoupled Cluster Segmentation

The second presented method aims to improve the segmentation accuracy in saturated frames by exploiting intensity information and linear appearance of overlapping tracks. To achieve this purpose, multiple algorithms are employed in a decoupled scheme to propose and gradually refine segmentation into its final form. For initialization, a conventional morphological method is used. Clusters are then independently analyzed by Hough Transform [6] to detetermine the likelihood of insufficient partitioning, and to produce secondary segmentation if necessary.

Hough Transform is a computer vision method often used for recognition of complex parametric shapes and patterns (e.g. lines, circles, etc.). Its major advantages include efficient tractability in 2D and robustness

Algorithm 1 RANSAC, LO-RANSAC and SA-RANSAC

$r_{\max} \leftarrow$ maximum number of iterations
$U^* \leftarrow -\infty$, $r \leftarrow 1$
repeat
    Select pixel coordinates $\vec{a}^r, \vec{b}^r$ at random.
    Fit model $\mathcal{M}^r$ from $\vec{a}^r, \vec{b}^r$.
    Evaluate the utility of the model $U^r \leftarrow U_{w,\Phi}(\mathcal{M}^r \mid F)$.
    if $U^r > U^*$ **then**
        Improve $U^* \leftarrow U^r$, $\mathcal{M}^* \leftarrow \mathcal{M}^r$ (with the help of no / greedy / SA optimizer).
    $r \leftarrow r + 1$
until $r \geq r_{\max}$

towards relatively large amount of input noise. In the presented algorithm, a version capable of detecting lines is utilized with the motivation to recognize integrated track overlaps and piecewise linear prongs. To avoid problems caused by possibly unbounded values of conventional linear parameterizations, the transform uses *Hesse normal form* which parameterizes lines as:

$$r = x_1 \cos\theta + x_2 \sin\theta \qquad \text{where } \theta \in [0, \pi], r \in [-r_{\max}, r_{\max}] \tag{2}$$

In a modified algorithm (given by Algorithm 2), after the accumulator is populated with votes from each pixel of the analyzed cluster, global maxima addressed by θ and r are identified in the accumulator. Each such maximum represents a linear fragment of the cluster, and is removed along with its local neighborhood both from the cluster and the accumulator. This way, duplicate detections are prevented without the necessity for subsequent non-maxima suppression. This process continues sequentially until the value of the maximum falls below an adjustable threshold.

Algorithm 2 Segmentation Refinement by Hough Transform

$A_{\min} \leftarrow$ accumulator termination threshold, $s_{\max} \leftarrow$ maximum number of iterations
$A \leftarrow$ empty accumulator, $s \leftarrow 1$
for $(x, e) \in F$ **do** ▷ Each pixel votes for all lines consistent with it.
    for $(\theta, r) \in \mathcal{L}(x)$ **do**
        Cast vote $A(\theta, r) \leftarrow A(\theta, r) + \Phi(e)$.
repeat ▷ Most likely maxima are sequentially removed.
    $(\theta^s, r^s) \leftarrow \operatorname{argmax}_{(\theta,r)} A(\theta, r)$
    $A^s \leftarrow A(\theta^s, r^s)$
    $C_s \leftarrow \{(x, e) \in F \mid x \text{ consistent with } (\theta^s, r^s)\}$
    for $(x, e) \in C_s$ **do** ▷ Votes for the removed line are subtracted.
        for $(\theta, r) \in \mathcal{L}(x)$ **do**
            Suppress inlier vote $A(\theta, r) \leftarrow A(\theta, r) - \Phi(e)$.
    Report subset C_s.
    $s \leftarrow s + 1$
until $A^s \leq A_{\min}$ or $s \geq s_{\max}$

2.3 Particle Identification

The goal of the third presented method is to achieve particle identification (PID) by sampling and aggregating intensities from frames. This is motivated by the theory of energy deposition along the particle trajectory within a Timepix sensor. In general, this quantity was described by the Bethe-Bloch equation [17] as sensitive to the nuclear charge of the projectile and its velocity. To achieve classification capability, this relationship is exploited by a simple machine learning algorithm.

The stopping power is sampled from clusters across several uniform intervals along the particle trajectory (as fitted by e.g. RANSAC). Sampled energies with normalized ordering constitute a feature model, which is used to train a standard k-NN classifier [5]. With a sufficient number of examples, the classifier learns stopping powers of various particle classes, gaining the ability to label previously unobserved clusters by cross-referencing their features with internal representation of training data.

3 Results

For evaluation, both experimental and artificial datasets were utilized. Even though testing with experimental data is generally preferable as it provides valuable insight into behavior under realistic conditions, inherent lack of ground truth information complicates the quantification of spatial and angular accuracies. The generation of entirely artificial datasets (e.g. by means of a physics simulation) on the other hand fails to reproduce phenomena relevant to evaluated algorithms. For these reasons, a middle ground approach was selected, wherein experimental data were curated, manually annotated with approximate ground truth information and randomly combined, producing large artificial datasets of realistic Timepix frames.

The experimental data used was measured at the Heidelberg Ion Therapy Center[†] and Super Proton Synchrotron, CERN. The setup included a Timepix detector equipped with a 1 mm thick Si sensor layer. The bias voltage was set to 500 V and the acquisition time was set to 0.1 s. During the experiment, charged particles hit the detector at various angles. Each dataset hence corresponds to a specific beam configuration (particle species and momentum) and incidence angle. In the datasets, the following particle species are represented: p, He, C, O, Ar. To increase quality, measured datasets were first automatically processed to exclude corrupted, oversaturated and noisy frames. Out of several thousands remaining frames, the total of 937 ground truth tracks were manually prepared.

3.1 Randomized Trajectory Fitting

The first experiment examines the behavior of the presented RANSAC-inspired algorithms in a very basic setting comprised of frames containing only one track produced by a single particle. Although such a scenario is not likely to be often observed in reality, it is desirable for the purposes of evaluation. As the lack of overlaps renders segmentation unnecessary, it provides a valuable insight into the performance of proposed trajectory fitting methods.

For the experiment, 1,000 artificial frames were generated from the ground truth dataset. This quantity is considered to be a good compromise between tractability and accuracy. In each frame, a track was chosen uniformly at random, and placed at a random non-cropping location within the pixel matrix. To suppress directional bias, track orientation was randomized as well. However, in order to avoid intensity interpolation, the rotation angle was quantized to 90 degrees. Several examples of the generated frames are shown in Figure 2.

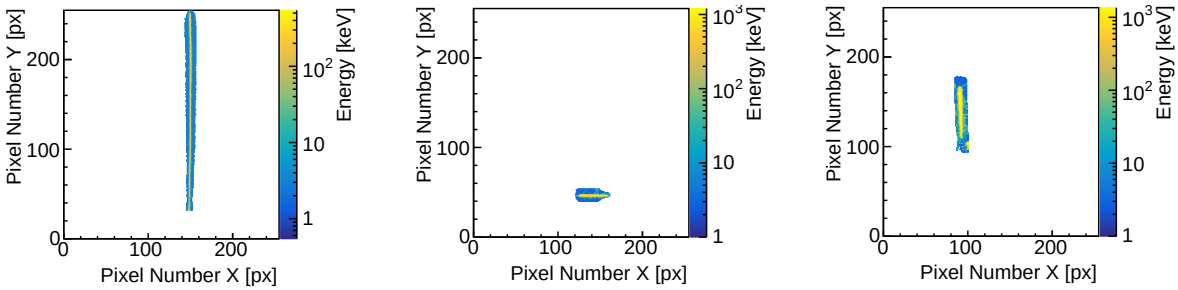

Figure 2: Selected artificial frames used for trajectory fitting evaluation.

[†]Heidelberger Ionenstrahl-Therapiezentrum (HIT), Im Neuenheimer Feld 450, 69120 Heidelberg, `https://www.klinikum.uni-heidelberg.de/index.php?id=113005&L=1`

In evaluation of the presented algorithms, two standard metrics are tracked – the failure rate FR and the error $E(v)$ of arbitrary parameter v. These metrics are conservatively defined as follows:

$$FR = \frac{FP + FN}{TP + TN + FP + FN} \qquad E(v) = \sqrt{\frac{1}{n}\sum_{i=1}^{n}(v_i - \hat{v}_i)^2} \tag{3}$$

Here, the values FP, FN, TP, TN refer to the numbers of false positive, false negative, true positive and true negative detections, respectively. Moreover, for $i = 1, 2, \ldots n$ the sequences $\hat{v}_i$ and v_i represent fitted parameters and their corresponding ground truth values, respectively. Since there is exactly one track in each frame, zero detections are regarded as a false negative, one detections as a true positive, and any further detections fits as false positives. To suppress random effects, each frame has been repeatedly processed 3 times. The results shown in Table 1 are mean values over all runs. The values of used configuration parameters are shown in Table 2.

Algorithm	$\langle FR \rangle$	$\langle E(a_1) \rangle$	$\langle E(a_2) \rangle$	$\langle E(\varphi) \rangle$	$\langle E(\theta) \rangle$	$\langle t \rangle$ [ms]
RANSAC	0.022	3.227	2.821	3.047	10.412	1,012.7
LO-RANSAC	0.021	2.898	2.873	2.886	11.863	5,538.6
SA-RANSAC	0.021	2.721	2.908	2.856	12.582	1,762.5

Table 1: Results of trajectory fitting evaluation.

3.2 Decoupled Cluster Segmentation

In the second experiment, the enhanced overlap segmentation capability of the presented decoupled segmentation algorithm was evaluated. In a familiar scheme, artificial datasets were randomly generated from manually annotated measured data. In this instance, however, the artificial frames contain varying numbers of overlapping tracks $n_{\text{trk}} \in \{5, 10, 20, 50\}$ (shown in Figure 3). These can be viewed as simulations taken with increasing acquisition time.

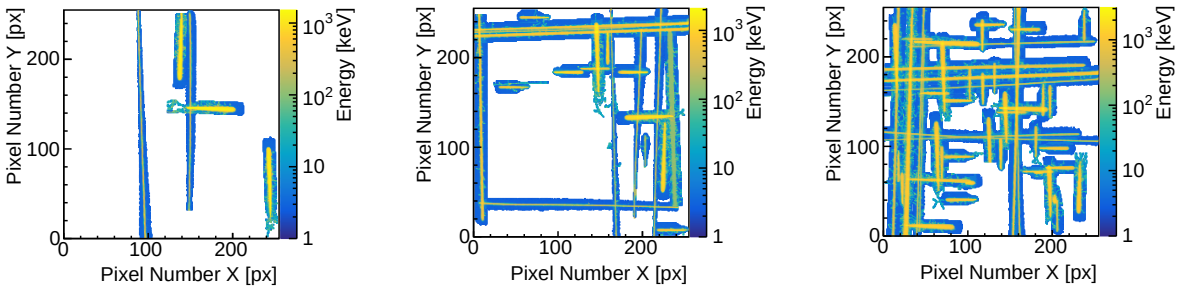

Figure 3: Selected artificial frames used for overlap segmentation evaluation with varying track counts. From left to right, $n = 5, 20, 50$ respectively.

In evaluation of every frame, a matching between ground truth detections and produced detections was constructed, wherein only detections with sufficiently small distance were matched. While successfully matched pairs were regarded as true positives, unmatched ground truth detections were treated as false negatives and unmatched detections provided were considered to be false positives.

To provide realistic insight into practical application of all presented methods, detections produced by Hough segmentation were additionally processed by RANSAC methods. This way, any systematic fitting bias introduced by the Hough method is amplified in contrast to the results of the previous experiment. Randomized evaluation was performed in the same scheme (1,000 frames, 3 runs each). The results as well as values of used configuration parameters are shown in Table 2.

	n_{trk}	$\langle FR \rangle$	$\langle E(a_1) \rangle$	$\langle E(a_2) \rangle$	$\langle E(\varphi) \rangle$	$\langle E(\theta) \rangle$	$\langle t \rangle$ [ms]
RANSAC	5	0.107	4.344	4.266	5.244	10.085	4,492.2
	10	0.253	6.413	6.384	9.030	10.826	9,123.3
	20	0.544	10.264	9.776	12.012	11.786	20,626.7
	50	0.772	14.852	14.572	14.655	10.226	38,161.3
LO-RANSAC	5	0.104	4.194	3.953	5.169	11.709	24,105.5
	10	0.242	6.096	6.219	8.549	12.250	57,995.2
	20	0.532	9.777	9.311	11.620	12.682	125,795.0
	50	0.770	14.034	13.888	13.960	10.167	294,498.0
SA-RANSAC	5	0.105	4.026	3.938	5.115	12.205	20,882.6
	10	0.238	6.088	6.064	7.833	12.539	19,708.4
	20	0.528	9.768	9.163	10.912	12.578	39,827.8
	50	0.769	14.324	14.111	12.535	9.892	83,365.4

RANSAC / LO-RANSAC / SA-RANSAC	
Parameter	Value
Energy Kernel Φ	ReLU
Distance Weight w	Gaussian
Sample Count	2,000
Connectivity Thl. e_0	10^{-3} keV
Neighborhood Size	8
L.O. Iterations	0 / 10^2 / 10^3
L.O. Window Δ	$\{0, \pm 0.2\}$
Annealing Schedule	0 / 0 / linear
H.T. Inlier Distance	7 pixels
H.T. Minimum Thl.	5,000
H.T. Iterations	100

Table 2: Results of overlap detection evaluation (left) and the configuration parameters used (right).

3.3 Particle Identification

To investigate the viability of the presented feature model for particle identification, the Heidelberg datasets were used once again. Unlike in previous sections, here ground truth information consists only of the particle species, a known property of the particle beam, eliminating any necessity for manual data labeling.

For evaluation, a stratified K-fold cross-validation scheme was adopted. The experimental data was randomly divided into 5 equally-sized folds, each containing approximately equal representation of all classes. In multiple runs, four folds were interpreted as the training set, whereas the fifth served as the testing set, producing a single accuracy score per run. Finally, the overall accuracy score was calculated as the mean of scores from all runs. This way, the effects of the hyperparamter n_{int} determining the number of sampling intervals were investigated for values $n_{\text{int}} \in \{1, 16, 32, 64, 128\}$. The calculated accuracies are shown in Table 3 and Figure 4.

n_{int}	$\langle t_{\text{train}} \rangle$ [ms]	$\langle t_{\text{test}} \rangle$ [ms]	$\langle$accuracy$\rangle$
1	0.906	1.054	0.851
16	0.645	1.917	0.893
32	1.023	5.315	0.892
64	2.051	6.065	0.885
128	1.901	11.225	0.887

c	$\langle t_{\text{train}} \rangle$ [ms]	$\langle t_{\text{test}} \rangle$ [ms]	$\langle$accuracy$\rangle$	$\langle$RR$\rangle$
0.50	1.208	2.481	0.895	0.006
0.75	0.731	2.325	0.922	0.111
0.90	0.620	1.612	0.935	0.249
0.95	0.721	2.398	0.935	0.249

Table 3: PID experiment results for varying sampling intervals (left) and confidence thresholds (right).

In order to achieve further accuracy improvement, measures were taken to minimize the number of misclassified samples by permitting the classifier to withhold decision in cases where errors are likely to occur. This is advantageous especially in applications where the effects of misclassification are less desirable than those of no classification at all. In implementation, the probability of a correct classification is commonly reflected by a confidence measure, which is thresholded at a constant level. For k-NN classifiers, this confidence is conservatively defined as k^j/k where $k = 7$ is the number of nearest neighbors and k^j denotes the number of training samples from the class y^j among the nearest neighbors in the scope of the current classification instance.

The effects of specific threshold values were examined by performing cross-validation for multiple constant values $c \in \{0.5, 0.75, 0.9, 0.95\}$. For all instances, the best-performing feature model with $n_{\text{int}} = 16$ was selected. In addition to accuracy, the rejection ratio (abbr. RR) was tracked to illustrate the overall confidence in classified samples at various thresholds. Lastly, the calculation of accuracy was constrained to accepted classifications only. Results of the experiment are shown in Table 3 and Figure 4.

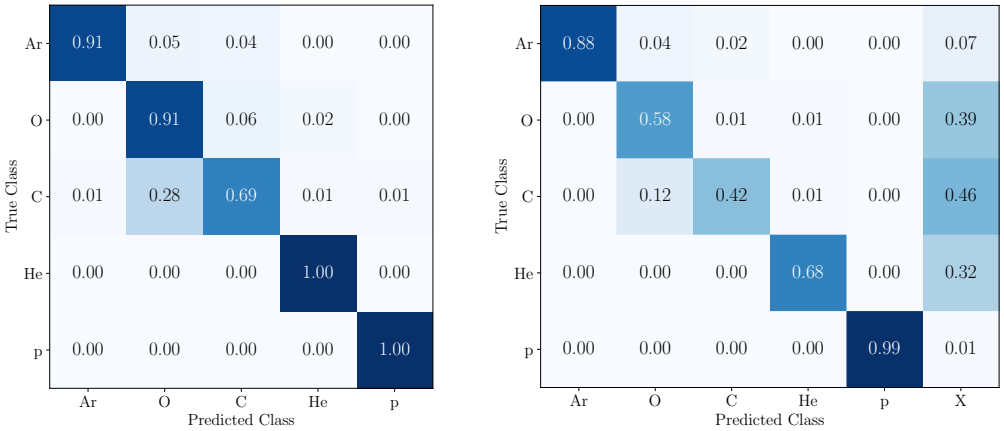

Figure 4: Confusion matrices of the k-NN classifier ($k = 7$, $n_{\text{int}} = 16$) without rejection (left, accuracy = 0.893) and with rejection (right, $c = 0.9$, accuracy = 0.935, RR = 0.249).

4 Conclusions

In this work, new analysis methods of Timepix frames were introduced and evaluated. The proposed algorithms update and extend older morphological methods with modern approaches, utilizing ToT information for better accuracy and increased performance. Based on commonly used computer vision methods, the presented algorithms are trans-dimensional and inherently robust to input noise.

In artificial Timepix frames produced from manually annotated experimental datasets, the presented algorithms proved to be viable for linear trajectory fitting, overlap separation and particle identification. On average, SA-RANSAC correctly identified the particle entry and exit points within 3 pixels (165 μm) and the azimuthal direction within 2.9 degrees. The modified Hough algorithm achieved predominantly correct results in frames with up to 20 overlaps. The PID feature model was accurate up to 0.893 without rejection and up to 0.935 with rejection rate below 0.25 at confidence threshold 0.9.

The presented algorithms for segmentation, trajectory reconstruction and particle identification are considered to be viable alternatives to conventional morphological methods, especially in high-flux environments where frame sparsity cannot be necessarily attained. Easily generalizing to 3D, the presented algorithms may find numerous applications in analysis related to Timepix and Timepix3 detectors (illustrated in Figure 5).

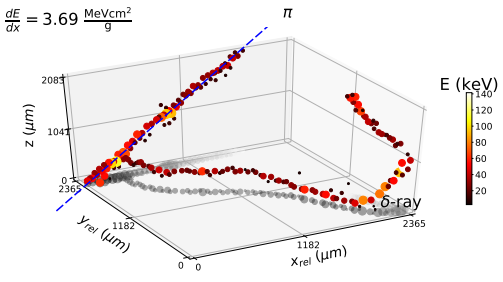

(a) 3D-reconstructed pion track observed by a Timepix3 detector, robustly fitted with a linear model (blue) using a generalized RANSAC method [4, 1].

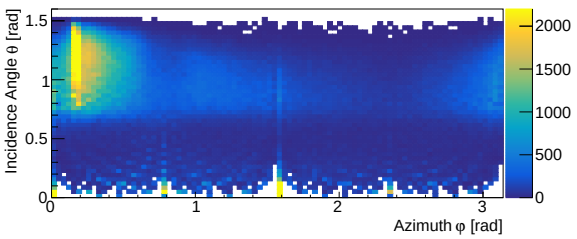

(b) Histogram of spatial directions fitted from 869,311 tracks observed on July 29-30, 2017 (LHC fill #6024) by a Timepix detector at MoEDAL Experiment, LHCb [16].

Figure 5: Selected applications of the presented analysis methods.

ACKNOWLEDGEMENTS

The authors would like to express their sincere gratitude to the Medipix2 and Medipix3 Collaboration for their permanent support. This work was supported by European Regional Development Funds: *"Van de Graaf Accelerator and Tunable Source of Monoenergetic Neutrons and Light Ions"* (No. CZ.02.1.02 / 0.0 / 0.0 / 16_013 / 0001785) and *"Research Infrastructure for Experiments at CERN"* (LM 2015058)

References

[1] B. Bergmann, P. Burian, P. Mánek, and S. Pospisil. 3D reconstruction of particle tracks in a 2 mm thick CdTe hybrid pixel detector. *The European Physical Journal C*, 79(2):165, 2019.

[2] B. Bergmann, I. Caicedo, C. Leroy, S. Pospisil, and Z. Vykydal. ATLAS-TPX: a two-layer pixel detector setup for neutron detection and radiation field characterization. *Journal of Instrumentation*, 11(10):P10002, 2016.

[3] B. Bergmann, C. Granja, A. Owens, M. Pichotka, S. Polansky, S. Pospisil, et al. Measurement of particle directions in low earth orbit with a Timepix. *Journal of Instrumentation*, 11(11):C11023, 2016.

[4] B. Bergmann, M. Pichotka, S. Pospisil, J. Vycpalek, P. Burian, P. Broulim, and J. Jakubek. 3D track reconstruction capability of a silicon hybrid active pixel detector. *The European Physical Journal C*, 77(6):421, 2017.

[5] T. Cover and P. Hart. Nearest neighbor pattern classification. *IEEE transactions on information theory*, 13(1):21–27, 1967.

[6] R. O. Duda and P. E. Hart. Use of the Hough transformation to detect lines and curves in pictures. Technical report, SRI INTERNATIONAL MENLO PARK CA ARTIFICIAL INTELLIGENCE CENTER, 1971.

[7] R. Filgas. Space radiation monitoring with Timepix. *Astronomische Nachrichten*, 339(5):386–390, 2018.

[8] M. A. Fischler and R. C. Bolles. Random sample consensus: a paradigm for model fitting with applications to image analysis and automated cartography. *Communications of the ACM*, 24(6):381–395, 1981.

[9] S. Gohl, B. Bergmann, H. Evans, P. Nieminen, A. Owens, and S. Posipsil. Study of the radiation fields in LEO with the Space Application of Timepix Radiation Monitor (SATRAM). *Advances in Space Research*, 63(5):1646–1660, 2019.

[10] B. Hartmann, K. Gwosch, C. Granja, J. Jakubek, S. Pospíšil, O. Jäkel, and M. Martišíková. Towards fragment distinction in therapeutic carbon ion beams: A novel experimental approach using the Timepix detector. In *2012 IEEE Nuclear Science Symposium and Medical Imaging Conference Record (NSS/MIC)*, pages 4076–4079. IEEE, 2012.

[11] T. Holy, E. Heijne, J. Jakubek, S. Pospisil, J. Uher, and Z. Vykydal. Pattern recognition of tracks induced by individual quanta of ionizing radiation in Medipix2 silicon detector. *Nuclear Instruments and Methods in Physics Research Section A: Accelerators, Spectrometers, Detectors and Associated Equipment*, 591(1):287–290, 2008.

[12] J. Jakubek. Semiconductor pixel detectors and their applications in life sciences. *Journal of Instrumentation*, 4(03):P03013, 2009.

[13] J. Jakubek. Precise energy calibration of pixel detector working in time-over-threshold mode. *Nuclear Instruments and Methods in Physics Research Section A: Accelerators, Spectrometers, Detectors and Associated Equipment*, 633:S262–S266, 2011.

[14] S. Kirkpatrick, C. D. Gelatt, and M. P. Vecchi. Optimization by simulated annealing. *science*, 220(4598):671–680, 1983.

[15] X. Llopart, R. Ballabriga, M. Campbell, L. Tlustos, and W. Wong. Timepix, a 65k programmable pixel readout chip for arrival time, energy and/or photon counting measurements. *Nuclear Instruments and Methods in Physics Research Section A: Accelerators, Spectrometers, Detectors and Associated Equipment*, 581(1-2):485–494, 2007.

[16] P. Mánek. Machine learning approach to ionizing particle recognition using hybrid active pixel detectors, 2018.

[17] K. A. Olive, P. D. Group, et al. Review of particle physics. *Chinese Physics C*, 38(9):090001, 2014.

[18] J. Pinfold. The MoEDAL experiment at the LHC. In *EPJ Web of Conferences*, volume 145, page 12002. EDP Sciences, 2017.

[19] T. Poikela, J. Plosila, T. Westerlund, M. Campbell, M. De Gaspari, X. Llopart, V. Gromov, R. Kluit, M. van Beuzekom, F. Zappon, et al. Timepix3: a 65k channel hybrid pixel readout chip with simultaneous toa/tot and sparse readout. *Journal of instrumentation*, 9(05):C05013, 2014.

[20] P. Soukup, J. Jakubek, M. Martisikova, M. Kroupa, and S. Pospisil. Dynamics of charge collection in pixelated semiconductor sensor studied with heavy ions and timepix. In *2012 IEEE Nuclear Science Symposium and Medical Imaging Conference Record (NSS/MIC)*, pages 4184–4187. IEEE, 2012.

[21] N. Stoffle, L. Pinsky, M. Kroupa, S. Hoang, J. Idarraga, C. Amberboy, R. Rios, J. Hauss, J. Keller, A. Bahadori, et al. Timepix-based radiation environment monitor measurements aboard the International Space Station. *Nuclear Instruments and Methods in Physics Research Section A: Accelerators, Spectrometers, Detectors and Associated Equipment*, 782:143–148, 2015.

[22] D. Turecek, L. Pinsky, J. Jakubek, Z. Vykydal, N. Stoffle, and S. Pospisil. Small dosimeter based on Timepix device for International Space Station. *Journal of Instrumentation*, 6(12):C12037, 2011.